# Image-Domain Q Inversion

*Yuqing Chen*[1] *, Gaurav Dutta*[1] *and Gerard T. Schuster*[1]
[1] *King Abdullah University of Science and Technology (KAUST), Thuwal 23955-6900, Kingdom of Saudi Arabia.*

## SUMMARY

Seismic waves traveling in the earth experience amplitude loss and velocity dispersion associated with strong subsurface attenuation. To compensate for these effects, the Q model should be first estimated and the data can be corrected. However, Q estimation from the data can be challenging if the data have a poor signal-to-noise ratio. To mitigate this problem, we develop a wave-equation Q inversion method in the image domain. This method seeks a Q model which minimizes the local wavenumber differences between a reference image without Q effects, and a Q migration image computed with the current Q model. Numerical tests on synthetic data demonstrate that the Q model inverted by this image-domain Q inversion method can lead to a noticeable improvement in the migration image quality.

## INTRODUCTION

Strong subsurface attenuation can significantly distort the amplitudes and phases of seismic waves (Aki and Richards, 1980). This attenuation can be quantified by a quality factor Q that accounts for the phase-shift and the amplitude loss as a function of the frequency and distance traveled by the propagating waves. Lower Q values indicate higher attenuation, which means greater energy loss per cycle of wave propagation.

To account for attenuation, Dai and West (1994), Yu et al. (2002), Wang (2007) and Valenciano et al. (2011) used the one-way wave-equation migration in the frequency domain for attenuation compensation. For reverse time migration, Zhang et al. (2010), Suh et al. (2012), Fletcher et al. (2012), Zhu et al. (2014) and Zhu and Harris (2015) proposed different viscoacoustic wave equations with separate controls over phase and amplitude to compensate for attenuation loss. Dutta and Schuster (2014), Sun et al. (2015), and Dai et al. (2015), Chen et al. (2017) used viscoacoustic least-squares reverse time migration (Q-LSRTM) schemes to compensate for the amplitude loss and phase distortion during migration.

Reliable velocity and Q models are both needed for accurate Q-compensated migration. A Q model can be estimated using either data-domain or image-domain tomographic techniques. In the data domain, Quan and Harris (1997) used the centroid-frequency shifts between the predicted and the observed traces and smeared the shifts along raypaths to update the Q model. For full waveform inversion (FWI)-like algorithm, Bai et al. (2013) used the waveform difference between the observed and predicted data to invert for the Q model. However, FWI-like algorithms often suffer from the cycle skipping problem and amplitudes can be altered by other factors such as scattering, interference from other events, or changes in impedance. To alleviate these problems, Dutta and Schuster (2016) used a skeletonized wave-equation Q inversion method that finds the Q model that minimizes the differences between the peak frequencies of the observed and the predicted transmission arrivals.

Data-domain methods become challenging when the data suffer from a low signal-to-noise ratio, diffractions and interference from many events. On the other hand, the image-domain methods are less prone to these issues, because the crossing events in the data are separated in the migration image and the stacking employed by migration suppresses the noise. Shen et al. (2014) used the spectral-ratio method to compute the differences between a Q-image and an attenuation-free target image, which is attenuation-free, and then related the image differences to the perturbation in the Q model based on migration velocity analysis. In this case, the implicit assumption is that only the Q model accounts for variations in the perturbed amplitudes.

In this paper, I present an image-domain skeletonized wave-equation Q inversion method that inverts for the Q model that minimizes the vertical-wavenumber differences between a Q-migration image and its attenuation-free reference image. The reference image is computed in three steps: (1) picking of the position of several reflectors in the Q-image, (2) followed by acoustic Born-modeling using these picked reflectors to generate the Born data and (3) finally acoustic migration of the Born data. By using the skeletonized misfit function, this method is less prone to the cycle skipping problem.

This paper is divided into 4 sections. After the introduction, the second section presents the theory of image-domain Q inversion. Numerical tests on synthetic data are presented in the third section, and the last section summarizes our results.

## THEORY

The objective function $\varepsilon$ for the image-domain Q inversion method is

$$\varepsilon = \frac{1}{2}\sum_{\mathbf{x}_0 \in \mathbf{B}} \Delta k_z(\mathbf{x}_0)^2, \tag{1}$$

where $\Delta k_z(\mathbf{x}_0)$ is the difference of the peak/centroid vertical wavenumber between two patches $B(\mathbf{x}_0)$ centered at $\mathbf{x}_0$ of a Q-migration image and a reference image $m_0$. $\mathbf{B}$ stands for the set of all patches in the migration image. The Q migration image $m_Q$ is obtained by migrating the observed data $d^{obs}$ using the current Q model. We then pick the position of several reflectors from $m_Q$, calculate the data using these picked reflectors as input to the acoustic Born modeling operator, and migrate these data to obtain the reference image $m_0$. Note that



10.1190/segam2018-2997203.1

$m_0$ is unaffected by the Q model because the Born modeling and migration used to compute $m_0$ are based on the acoustic wave-equation without Q effects.

The gradient of the objective function $\varepsilon$ with respect to the relaxation parameter $\tau$ is given by

$$\frac{\partial \varepsilon}{\partial \tau(\mathbf{x}')} = \sum_{\mathbf{x}_0 \in \mathbf{B}} \frac{\partial \Delta k_z(\mathbf{x}_0)}{\partial \tau(\mathbf{x}')} \Delta k_z(\mathbf{x}_0), \tag{2}$$

where $\tau$ is the relaxation parameter which is related to the quality factor Q by

$$\tau = \frac{2}{Q}\left(\frac{1}{Q} + \sqrt{1+\frac{1}{Q^2}}\right). \tag{3}$$

Here, we choose to invert for the relaxation parameter $\tau$ because it is quite sensitive to the small changes in Q (Dutta and Schuster, 2016).

In order to calculate the Fréchet derivative of $\Delta k_z(\mathbf{x}_0)$ with respect to the relaxation parameter $\tau$ perturbation at $\mathbf{x}'$, a connective function is defined as the local inner product between $m_0(B(\mathbf{x}_0))$ and $m_Q(B(\mathbf{x}_0))$:

$$F(k_z', \tau(\mathbf{x}')) = \sum_{\mathbf{x} \in B(\mathbf{x}_0)} m_0(k_z - k_z', \mathbf{x}) m_Q(k_z, \mathbf{x}), \tag{4}$$

where $k_z'$ is an arbitrary vertical wavenumber shift. For an accurate Q model, the wavelet stretch effects in $m_Q$ will be compensated, then these two images will have the same peak vertical wavenumber within $B(\mathbf{x}_0)$. In other words, we seek a shift $k_z' = \Delta k_z$ that maximizes the product in equation 4. This means that the derivative of $F$ with respect to $k_z'$ should be zero at $\Delta k_z$:

$$\begin{aligned} \dot{F}(k_z', \tau(\mathbf{x}')) &= \sum_{\mathbf{x} \in B(\mathbf{x}_0)} \frac{\partial F(k_z', \tau(\mathbf{x}'))}{\partial k_z'}\Big|_{k_z' = \Delta k_z} \\ &= \sum_{\mathbf{x} \in B(\mathbf{x}_0)} \dot{m}_0(k_z - \Delta k_z, \mathbf{x}) m_Q(k_z, \mathbf{x}) \\ &= 0, \end{aligned} \tag{5}$$

where the dot represents the derivative with respect to $k'$.

The implicit function theorem gives

$$\frac{\partial \Delta k(\mathbf{x}_0)}{\partial \tau(\mathbf{x}')} = -\frac{\partial \dot{F}/\partial \tau(\mathbf{x}')}{\partial \dot{F}/\partial \Delta k(\mathbf{x}_0)}, \tag{6}$$

where the denominator is given by

$$\frac{\partial \dot{F}}{\partial \Delta k_z(\mathbf{x}_0)} = \sum_{\mathbf{x} \in B(\mathbf{x}_0)} \ddot{m}_0(k_z - \Delta k_z, \mathbf{x}) m_Q(k_z, \mathbf{x}). \tag{7}$$

Here, the double dots represent the second-order derivative with respect to $k_z'$.

Assuming only $m_Q$ is a function of the relaxation parameter $\tau$, the numerator of equation 6 is

$$\frac{\partial \dot{F}}{\partial \tau(\mathbf{x}')} = \sum_{\mathbf{x} \in B(\mathbf{x}_0)} \dot{m}_0(k_z - \Delta k_z, \mathbf{x}) \frac{\partial m_Q(k_z, \mathbf{x})}{\partial \tau(\mathbf{x}')}. \tag{8}$$

Inserting equations 6, 7 and 8 into equation 2 yields

$$\frac{\partial \varepsilon}{\partial \tau(\mathbf{x}')} = -\sum_{\mathbf{x}_0 \in \mathbf{B}} \frac{\sum_{\mathbf{x} \in B(\mathbf{x}_0)} \Delta k_z(\mathbf{x}_0) \dot{m}_0(k_z - \Delta k_z, \mathbf{x}) \frac{\partial m_Q(k_z, \mathbf{x})}{\partial \tau(\mathbf{x}')}}{\sum_{\mathbf{x} \in B(\mathbf{x}_0)} \ddot{m}_0(k_z - \Delta k_z, \mathbf{x}) m_Q^k(\mathbf{x})}. \tag{9}$$

Substituting the Fréchet derivative $\frac{\partial m_Q(\mathbf{x})}{\partial \tau(\mathbf{x}')}$ derived in Appendix A into equation 9, the gradient of the objective function is

$$\frac{\partial \varepsilon}{\partial \tau(\mathbf{x}')} = \sum_{\mathbf{x}_0 \in \mathbf{B}} \frac{\sum_{\mathbf{x} \in B(\mathbf{x}_0)} (g_1 + g_2)}{\sum_{\mathbf{x} \in B(\mathbf{x}_0)} \ddot{m}_0(k_z - \Delta k_z, \mathbf{x}) m_Q(k_z, \mathbf{x})}, \tag{10}$$

where

$$\begin{aligned} g_1 &= \langle \frac{\partial \mathbf{S}}{\partial K}\mathbf{w}, (\mathbf{S}^*)^{-1} \frac{\partial \mathbf{S}^*}{\partial \tau}\mathbf{w}^* \Delta m \rangle, \\ g_2 &= \langle \frac{\partial \mathbf{S}^*}{\partial K}\mathbf{w}^*, \mathbf{S}^{-1} \frac{\partial \mathbf{S}}{\partial \tau}\mathbf{w} \Delta m \rangle, \end{aligned} \tag{11}$$

in which $\Delta m(\mathbf{x}) = \Delta k_z(\mathbf{x}_0) \dot{m}_0(k_z - \Delta k_z, \mathbf{x})$. Here, $\mathbf{S}$ and $\mathbf{w}$ are the modeling operator and backgroud wavefield, respectively. $\mathbf{S}^*$ and $\mathbf{w}^*$ represent the adjoint modeling operator and the adjoint wavefield, respectively. $K$ denotes the bulk modulus of the medium.

The gradient in equation 10 has two terms. The first term $g_1$ corresponds to the source-side reflction wavepath, which is the dot product at $\mathbf{x}'$ between the downward-propagated source-side wavefield $\frac{\partial \mathbf{S}}{\partial K}\mathbf{w}$ and the upward-propagated receiver-side wavefield. The upward propagated receiver-side wavefield is generated by a virtual source at the image point $\mathbf{x}$, which is redatumed from the receivers at the surface. Similarly, the second term $g_2$ can be interpreted as the receiver-side reflection wavepath, which is the dot product at $\mathbf{x}'$ between the downward-propagated receiver-side wavefield $\frac{\partial \mathbf{S}^*}{\partial K}\mathbf{w}^*$ and the upward-propagated source-side wavefield. The upward source-side wavefield is excited by a virtual source at the image point $\mathbf{x}$, which is redatumed from the sources at the surface. The relaxation parameter is updated by smearing the energy of the local wavenumber shifts at $\mathbf{x}$ along the wavepaths associated with the sources and receivers.

Given the gradient, the steepest-descent method can be used to iteratively update the relaxation parameter until the peak vertical wavenumber shifts between two images are sufficiently small.

## NUMERICAL RESULTS

The effectiveness of the image-domain Q inversion method is now demonstrated with synthetic data generated from a single-layer model and the Marmousi Model. In addition, we also apply this method to the benchmark viscoacoustic data released by Schlumberger for the BP2004Q model.

### Single Layer Model

The effectiveness of image-domain Q inversion is now demonstrated with a single-layer model. Figure 1a depicts the true Q model, which has two rectangular Q anomalies of 0.04 and 0.025 embedded in an almost non-attenuative medium ($Q = 0.0001$). This Q model and a homogeneous velocity distribution (4000 m/s) with a reflectivity model which has a horizontal reflector at z=900 m, is used to generate the observed data. There are 98 shots with 398 receivers per shot uniformly distributed on the top boundary. The source wavelet is a Ricker wavelet with a central frequency of 40-Hz. The Q image $m_Q$ shown in Figure 1b is obtained by migrating the lossy observed data using the initial Q model and the correct velocity model, which shows some distortions caused by these Q anomalies. The red-dashed line in Figure 1b indicates the location of the picked reflectivity which is then used to compute the reference image $m_0$. The perturbed image $\Delta m$ is computed by perturbing the vertical wavenumber difference $\Delta k_z$ between $m_0$ and $m_Q$. The gradient used for updating the Q model can be constructed by using the perturbed image with equation 10.

Figure 2a shows the inverted 1/Q model which mostly agrees with the true model. The recovered migration image which is obtained by migrating the lossy data with the inverted Q model is shown in Figure 2b. In this example, the distortions are mitigated in this image. Figure 3 shows the wavenumber spectrum of a vertical slice at $x = 1280$ m for the migration images shown in Figures 1b and 2b. The spatial resolution of the image is improved after attenuation compensation using the inverted Q model.

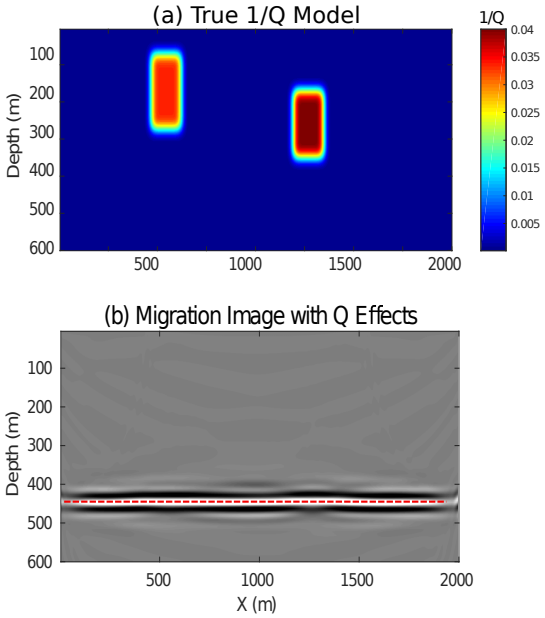


Figure 1: The (a) true Q model with 2 anomalies and (b) Q migration image. The red dashed line indicates the picked reflector used for estimating the reference image $\mathbf{m}_0$

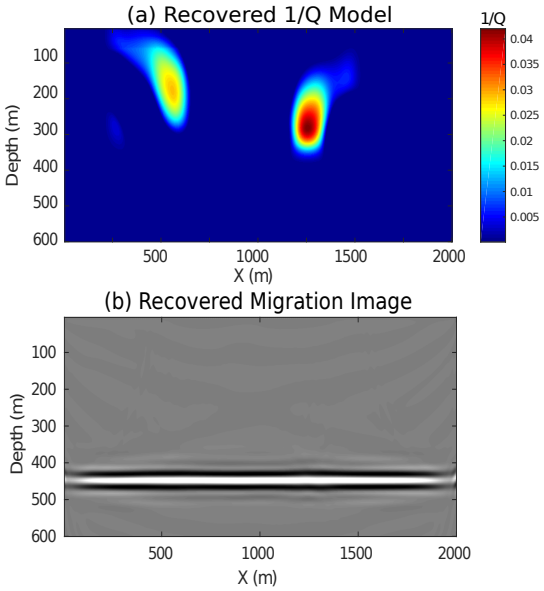


Figure 2: (a) The inverted 1/Q model and (b) the recovered migration image.

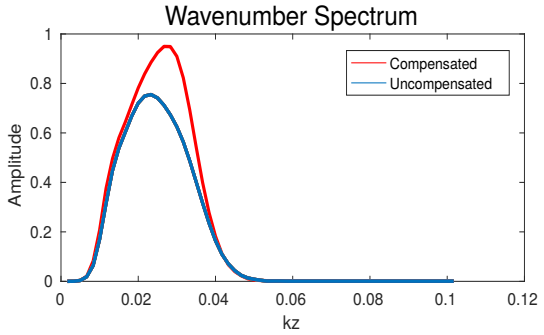


Figure 3: The $k_z$ wavenumber spectrum of a vertical slice at $x = 1280$ m in the two migration images shown in Figure 1b and 2b.

### Marmousi Model

The image-domain Q inversion method is now tested on the Marmousi Model. Figures 4a and 4b show the true velocity model and Q models, respectively, used for generating the observed data. There are two strong rectangular attenuation anomalies embedded in an almost non-attenuative medium. A Ricker wavelet with a peak-frequency of 15-Hz is used as the source wavelet. A fixed-spread acquisition geometry is used where 143 sources are evenly distributed on the surface at an interval of 20 m. The data are recorded by 287 receivers for each shot uniformly distributed every 10 m on the surface.

Figure 4c shows the Q migration image which is obtained by migrating the lossy observed data with the initial Q model, which is a homogeneous Q model with Q = 10000. The red dashed line in Figure 4c indicates the picked reflector. The inverted Q model is shown in Figure 5a where these two Q anomalies are successfully reconstructed. The distortions caused by low-Q anomalies are mitigated in the recovered migration shown in Figure 5b, which is computed by migrating the lossy data with the inverted attenuation model. Figure 6 shows the



10.1190/segam2018-2997203.1

wavenumber spectrum of a vertical slice at $x = 760$ m in Figures 4c and 5b. Attenuation compensation using the inverted Q model recovers the high frequencies loss.

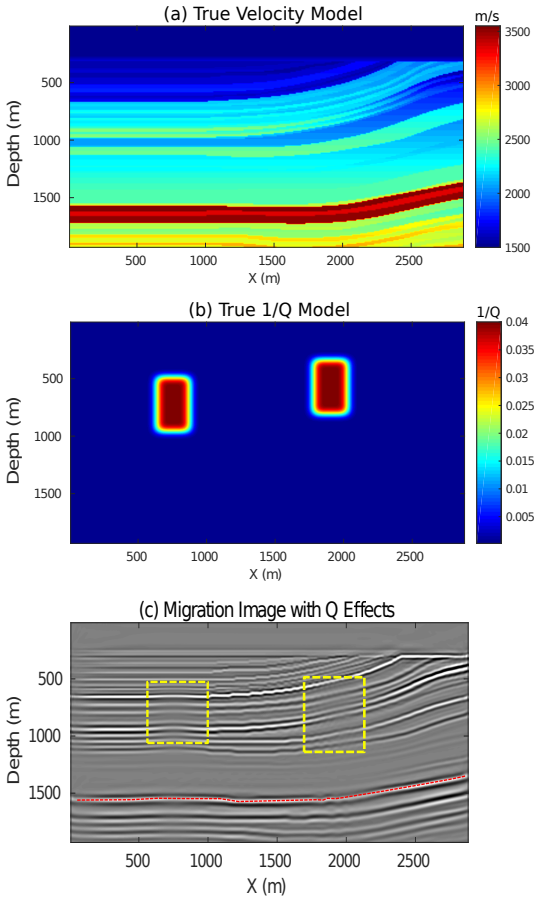


Figure 4: The (a) true velocity model, (b) true 1/Q model and (c) Q migration image. The red-dashed line indicates the picked reflector used for estimating the reference image $\mathbf{m}_0$

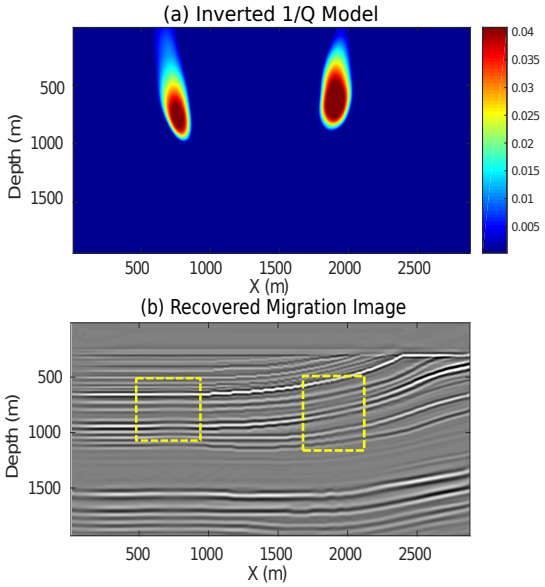


Figure 5: (a) The inverted 1/Q model and (b) recovered migration image.

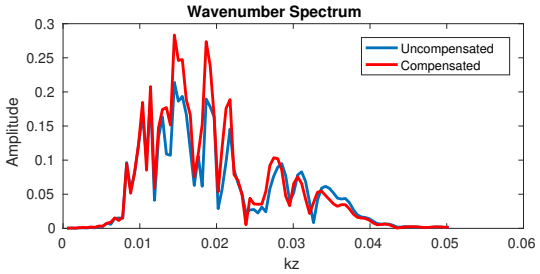


Figure 6: The $k_z$ wavenumber spectrum of a vertical slice at $x = 760$ m in Figures 4c and 5b.

## SUMMARY AND CONCLUSIONS

An image-domain Q inversion method is presented which inverts for the Q model from a skeletonized representation of the migration image. The skeletonized data are represented by the vertial wavenumber $k_z$ differences between the Q migration image and the reference image. The gradient of the image-domain Q inversion method is derived using the implicit function theorem and the update for the Q model at each iteration is computed by smearing the energy of the local wavenumber shifts along the wavepaths for each source-receiver pair. The input requirement is an accurate estimate of the background velocity model, which can be obtained by a conventional velocity analysis method. The next step is to apply this algorithm to more complicated synthetic data and field data. It will be interesting to assess the benefits and limitations of simultaneous inverting for both Q and velocity models using MVA. The limitation of this method is that the size of the inverted Q-anomaly is not always similar to the true model. This is due to the low resolution of the reflection inversion which can only update the average effects of these attenuation anomalies.

## ACKNOWLEDGMENTS

We thank the sponsors of the CSIM consortium, the KAUST Supercomputing Laboratory and IT Research Computing Group.

## REFERENCES


Aki, K., and P. G. Richards, 1980, Quantitative seismology: Freeman Publication Co.

Bai, J., G. Chen, D. Yingst, and J. Leveille, 2013, Attenuation compensation in viscoacoustic reserve-time migration: 83rd Annual International Meeting, SEG, Expanded Abstracts, 3825–3830, https://doi.org/10.1190/segam2013-1252.1.

Chen, Y., G. Dutta, W. Dai, and G. T. Schuster, 2017, Q-least squares reverse time migration with viscoacoustic deblurring filters: Geophysics, **82**, no. 6, S425–S438, https://doi.org/10.1190/geo2016-0585.1.

Dai, N., and G. F. West, 1994, Inverse Q migration: 64th Annual International Meeting, SEG, Expanded Abstracts, 1418–1421, https://doi.org/10.1190/1.1822799.

Dai, W., Z. Xu, and R. Coates, 2015, Least-squares reverse time migration for visco-acoustic media: 85th Annual International Meeting, SEG, Expanded Abstracts, 3387–3391, https://doi.org/10.1190/segam2015-5922472.1.

Dutta, G., and G. T. Schuster, 2014, Attenuation compensation for least-squares reverse time migration using the viscoacoustic-wave equation: Geophysics, **79**, no. 6, S251–S262, https://doi.org/10.1190/geo2013-0414.1.

Dutta, G., and G. T. Schuster, 2016, Wave-equation Q tomography: Geophysics, **81**, no. 6, R471–R484, https://doi.org/10.1190/geo2016-0081.1.

Fletcher, R., D. Nichols, and M. Cavalca, 2012, Wavepath consistent effective Q estimation for Q-compensated reverse-time migration: 74th Annual International Conference and Exhibition, EAGE, Extended Abstracts.

Quan, Y., and J. M. Harris, 1997, Seismic attenuation tomography using the frequency shift method: Geophysics, **62**, 895–905, https://doi.org/10.1190/1.1444197.

Shen, Y., B. Biondi, R. Clapp, and D. Nichols, 2014, Wave-equation migration Q analysis: 84th Annual International Conference and Exhibition, EAGE, Extended Abstracts, 3757–3762.

Suh, S., K. Yoon, J. Cai, and B. Wang, 2012, Compensating visco-acoustic effects in anisotropic resverse-time migration: 82nd Annual International Conference and Exhibition, EAGE, Extended Abstracts, 1–5.

Sun, J., S. Fomel, and T. Zhu, 2015, Preconditioning least-squares RTM in viscoacoustic media by Q-compensated RTM: 85th Annual International Meeting, SEG, Expanded Abstracts, 3959–3965, https://doi.org/10.1190/segam2015-5880944.1.

Valenciano, A., N. Chemingui, D. Whitmore, and S. B. Dahl, 2011, Wave equation migration with attenuation and anisotropy compensation: 81st Annual International Meeting, SEG, Expanded Abstracts, 232–236, https://doi.org/10.1190/1.3627674.

Wang, Y., 2007, Inverse-Q filtered migration: Geophysics, **73**, no. 1, S1–S6, https://doi.org/10.1190/1.2806924.

Yu, Y., R. S. Lu, and M. M. Deal, 2002, Compensation for the effects of shallow gas attenuation with viscoacoustic wave-equation migration: 82nd Annual International Meeting, SEG, Expanded Abstracts, 2062–2065, https://doi.org/10.1190/1.1817107.

Zhang, Y., P. Zhang, and H. Zhang, 2010, Compensating for visco-acoustic effects in reverse-time migration: 80th Annual International Meeting, SEG, Expanded Abstracts, 3160–3164, https://doi.org/10.1190/1.3513503.

Zhu, T., and J. M. Harris, 2015, Improved seismic image by Q compensated reverse time migration: Application to cross-well field data, West Texas: Geophysics, **80**, no. 2, B61–B67, https://doi.org/10.1190/geo2014-0463.1.

Zhu, T., J. M. Harris, and B. Biondi, 2014, Q-compensated reverse-time migration: Geophysics, **79**, no. 3, S77–S87, https://doi.org/10.1190/geo2013-0344.1.